A new approach to enhance photocatalytic nitrogen fixation performance via phosphate-bridge: a case study of SiW_{12}/K-C_3N_4

Cailin Xiao, Ling Zhang, Kefu Wang, Haipeng Wang, Yuanyi Zhou, Wenzhong Wang*

State Key Laboratory of High Performance Ceramics and Superfine Microstructure, Shanghai Institute of Ceramics, Chinese Academy of Sciences, 1295 Dingxi Road, Shanghai 200050, PR China

ARTICLE INFO

ABSTRACT

Photocatalytic nitrogen fixation, as a low-cost and promising technology, needs efforts to explore the photocatalyst with high activity and stability. In this study, the polyoxometalate (POM) cluster of $[H_4SiO_{40}W_{12}]$ (SiW_{12}) has been successfully covalently combined with the KOH-modified graphitic carbon nitride nanosheets (K-C_3N_4) through the phosphate-bridged strategy. With POM acting as the co-catalyst, SiW_{12}/K-C_3N_4 nanocomposites show excellent photocatalytic nitrogen fixation efficiency ($353.2\,\mu M\,g^{-1}\,h^{-1}$) in water under light-irradiation. It can be ascribed to the enhanced separation efficiency of charge carriers through the formation of "phosphate-bridged" bonds between K-C_3N_4 and SiW_{12}, and the increased oxidation capacity of water by bridging SiW_{12}. Moreover, K doping and bridging SiW_{12} improves the adsorption and activation of nitrogen, which can be conductive to the reduction of nitrogen to ammonia. This work provides a feasible route to design and synthesize nanocomposite materials with exceptional performance for photocatalytic nitrogen fixation.

1. Introduction

Nitrogen fixation is the second most important chemical process in nature next to photosynthesis. Although 80% of the atmosphere is nitrogen, it is difficult to be used as a reactant [1], partially because dinitrogen (N_2) is a typically inert molecule due to the strong N≡N bond ($945\ kJ\,mol^{-1}$) [2]. Therefore, industrial ammonia synthesis (Haber–Bosch reaction) is generally carried out at high temperature (400–600 °C) and high pressure (20–40 MPa), which results in high energy consumption and carbon dioxide emission. Hence, artificial nitrogen fixation under milder conditions is of great significance from the perspectives of cost control and environmental protection [3–6].

Recently, photocatalysis has been seen as a potential technology in nitrogen fixation with solar energy being the driving force in the reaction process. However, there are several bottlenecks for photocatalytic N_2 fixation, which are mainly divided into the following points: (i) limited N_2 adsorption on the catalyst surface with poor activation efficiency [7]; (ii) sluggish emergence and transfer of proton for protonation processes [8]; (iii) photo-generated electron-hole pair recombination ahead of the six-electron transfer for nitrogen fixation reaction [9,10]. Furthermore, most photocatalytic nitrogen fixation at the ambient temperature requires the addition of sacrificial agents, which provide protons for nitrogen-fixing reaction [11–13]. For instance, the KOH-treated g−C_3N_4 (K-C_3N_4) showed high activity for

photocatalytic fixation of N_2, which is attributed to that K doping improves the adsorption and activation of N_2 by introducing more surface nitrogen defects, as well as promotes the desorption of ammonia [14]. However, it was highly dependent on CH_3OH as a proton source, since K-C_3N_4 could not provide the protons needed for nitrogen fixation from the water splitting. Hence, one of the keys for solar nitrogen fixation lies in seeking an efficient photocatalyst with good performance for oxidizing water to provide proton for nitrogen fixation.

Herein, polyoxometalates (POMs), which are highly redox-active and can undergo light-induced redox-processes, is introduced as co-catalyst with K-C_3N_4 to enhance the ability of oxidizing water and the adsorption and activation of N_2 [15–17]. In addition, phosphate anions, as one of the effective adhesives and electron transport chain, were covalently combining POMs with K-C_3N_4 to enhance the interaction and transportation of carries, since they could be strongly adsorbed onto the surfaces of oxides by substituting surface hydroxyl groups [18–22]. Thus, combining the advantages of components catalyst in this design, SiW_{12}/K-C_3N_4 was synthesized by phosphate-bridged method and a high nitrogen fixation efficiency ($353.2\,\mu M\,g^{-1}\,h^{-1}$) was achieved. This work presents a feasible route to design the nanocomposite materials with good performance for photocatalytic nitrogen fixation.

* Corresponding author.
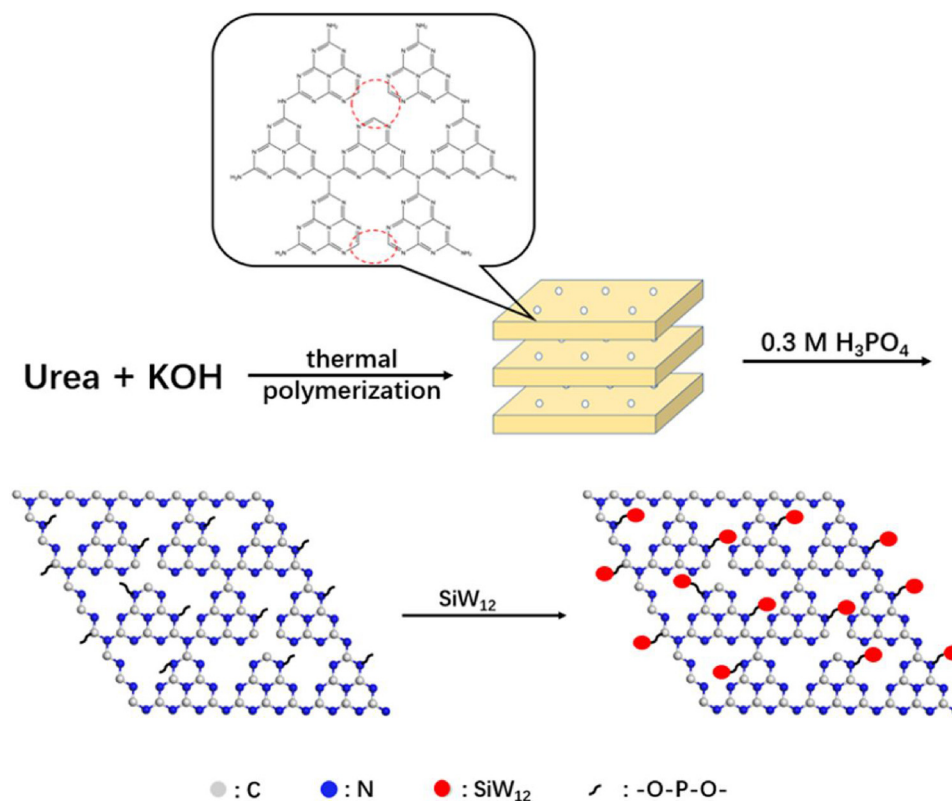 E-mail address: wzwang@mail.sic.ac.cn (W. Wang).

Fig. 1. Preparation process of SiW_{12}/K-C_3N_4.

2. Experimental

2.1. Materials synthesis

All reagents were of analytical purity and received from Shanghai Chemical Company without further purification.

2.1.1. Synthesis of g-C_3N_4 and K-C_3N_4 photocatalysts

Pristine g-C_3N_4 was prepared by urea pyrolysis according to a standard literature method. Briefly, 15 g of urea was calcined at 550 °C in a muffle furnace for 4 h using a heating rate of 10 °C·min^{-1}. K-C_3N_4 photocatalysts were synthesized as follows: 15 g of urea was dissolved with stirring into aqueous KOH solutions (0.01 g KOH dissolved in 30 mL of H_2O), and then the resulting solution was evaporated and dried in an oven at 80 °C overnight. The solid mixtures of urea and KOH were then calcined at 550 °C in a muffle furnace for 4 h with a heating rate of 10 °C·min^{-1}. After calcination, all samples were washed with water to remove any residual alkali [23].

2.1.2. Synthesis of SiW_{12}/K-C_3N_4 photocatalysts

SiW_{12} linked with K-C_3N_4 by using phosphate as a bridge. For the surface phosphating, K-C_3N_4 powder (0.1 g) was dispersed in an aqueous phosphoric acid (H_3PO_4) solution (0.3 M, 100 mL) and the suspension was stirred for 5 h for the adsorption of phosphate on the surface of K-C_3N_4. P-K-C_3N_4 powder (modified with phosphates of K-C_3N_4) was collected by filtration and then dried in an oven at 60 °C for 3 h and subsequently heat-treated in a furnace at 300 °C for 1.5 h. P-K-C_3N_4 was thoroughly washed with distilled water to remove weakly bound phosphate anions and dried in an oven at 60 °C. Then, a certain amount of SiW_{12} was added to the 30 mL absolute ethyl alcohol dispersion of P-K-C_3N_4 linker. After stirring for 2 h and dipping for 4 h, the hybrid catalyst of SiW_{12}/K-C_3N_4 was dried at 60 °C for 24 h.

2.2. Characterization

The as-prepared catalyst samples were characterized by powder X-ray diffraction (XRD) with a Rigaku D/MAX 2250 V diffractometer using monochromatized Cu Kα (λ = 0.15418 nm) radiation while the voltage and electric current were held at 40 kV and 100 mA, over the range of 5° ≤2θ ≤70°. Next, the powder was pressed into plates and the Fourier Transform Infrared (FTIR) spectra were carried out on a FTIR spectrometer (FTIR-7600, Lambda Scientific, Australia). X-ray photoelectron spectroscopy (XPS) was performed on an ESCALAB 250Xi, Thermo Scientific Ltd. with a 320 μm diameter spot of mono-chromated aluminum Kα X-rays at 1253.6 eV under ultrahigh-vacuum conditions. All binding energies were referenced to the C 1s peak (285 eV) arising from adventitious carbon. UV–vis diffuse reflectance spectra (DRS) of the samples were obtained on an UV–vis spectrophotometer (Hitachi U-3010) using $BaSO_4$ as the reference. Nitrogen temperature-programmed desorption (N_2-TPD) measurements were conducted on an Auto Chem II 2920 instrument. Usually, 100 mg of the sample, placed in a glass tube, was preconditioned by a He gas flow at 150 °C for 2 h, and then cooled down to 50 °C. The adsorption of N_2 was carried out in a 99.999% N_2 gas flow for 2 h at 50 °C. After purge by He gas, the sample was heated from 50 °C to 500 °C at a rate of 10 °C·min^{-1}. The TPD signal was recorded by a thermal conductivity detector. All the gas flow rates were set as 25 mL·min^{-1}.

2.3. Photocatalytic tests

Photocatalytic tests were performed under the irradiation of a Xe lamp (100 mW cm^{-2}). Typically, 50 mg of catalyst powder was uniformly dispersed in 200 mL of pure water by ultrasound. After irradiation with Xe light in N_2 for one hour, the NH_4^+ was measured by spectrophotometric method with Nessler's reagent.
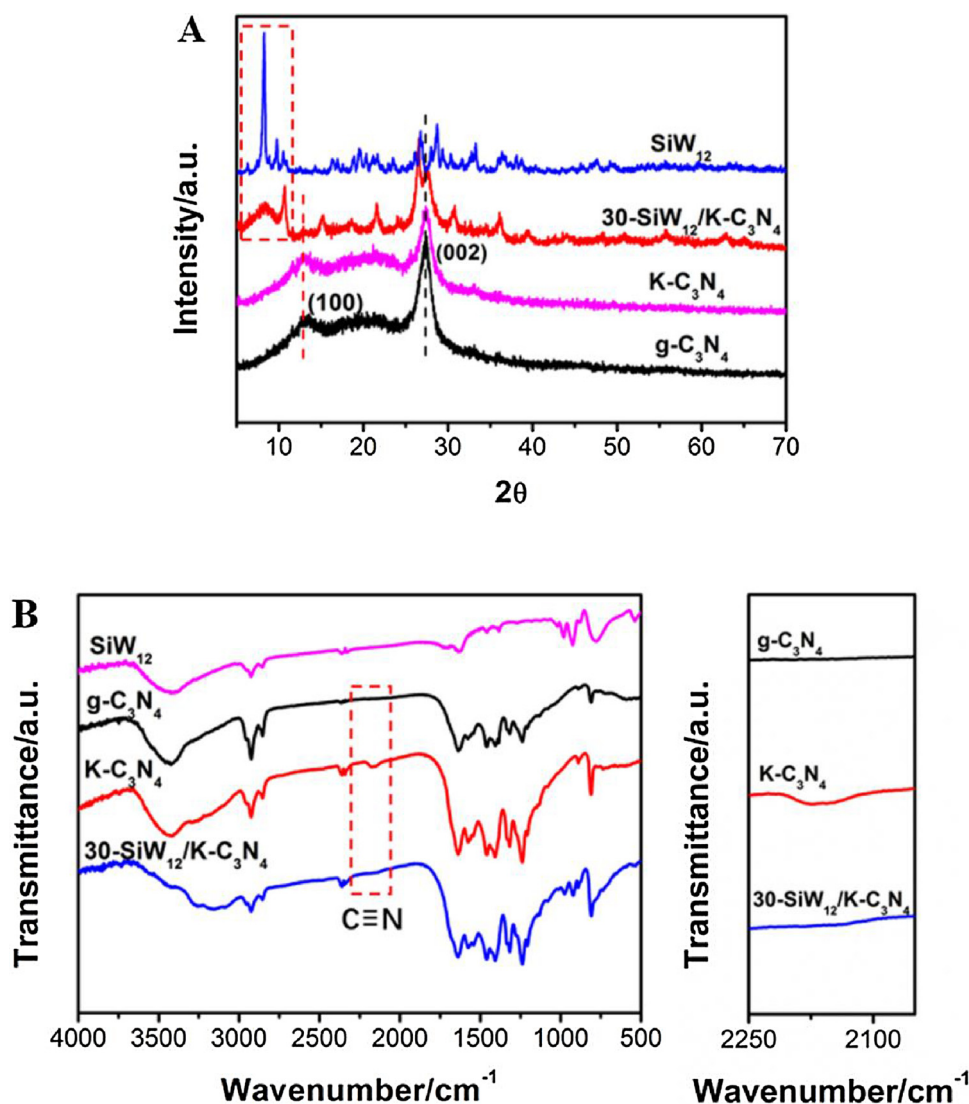
Fig. 2. (A) XRD patterns of pristine g-C_3N_4, K-C_3N_4, SiW_{12} and 30-SiW_{12}/K-C_3N_4; (B) FTIR spectra of bulk g-C_3N_4, K-C_3N_4, SiW_{12}, and 30-SiW_{12}/K-C_3N_4.

2.4. NH_3/NH_4^+ concentration analysis

Nessler's reagent method was used for NH_3/NH_4^+ concentration analysis. Firstly, 200 mL of the suspension was filtered through a 0.22 μm membrane filter and placed in a 50 mL sample tube. Next, 1 mL of the potassium sodium tartrate solution was added to the sample tube. After mixing evenly, 1 mL of Nessler's reagent was added to the same sample tube and blended. Then, the mixture was left to stand for 10 ~ 15 min for full color processing. Finally, the concentration of NH_3/NH_4^+ was measured using an UV–vis spectrophotometer (Hitachi U-3010) at 420 nm wavelength.

2.5. Electrochemical analysis

Electrochemical analysis was conducted on a CHI 660D electrochemical workstation (Shanghai Chenhua, China) using a standard three-electrode quartz cell, the counter electrode platinum wire and a reference electrode saturated calomel electrode (SCE). A Xe lamp (CHF-XM500) was used as light source. The working electrodes were prepared by dip-coating: catalyst powders were deposited on a fluorine-doped tin oxide (FTO) substrate about 1.5 cm × 2.5 cm square. Briefly, 10 mg of catalyst was suspended in 1 mL ethanol solution and the mixtures were ultrasonically scattered for 30 min to form slurry. Then,

100 μL of above slurry was coated on the FTO glass, and the ethanol was naturally evaporated under mild conditions and then calcined at 120 °C for 2 h. The catalyst coated FTO substrate was used as the working electrode. The current–time curves were collected at 0.2 V vs. SCE. Here, the electrolyte solution was 0.25 M Na_2SO_4 solution (pH = 6.8).

3. Results and discussion

3.1. Characterization of SiW_{12}/K-C_3N_4

As shown in Fig. 1, the covalent combination of POM cluster of SiW_{12} and K-C_3N_4 has been achieved by taking the phosphate-bridged strategy. The chemical structure of pristine g-C_3N_4, K-C_3N_4, SiW_{12} and a series of X-SiW_{12}/K-C_3N_4 powders (X represents the SiW_{12} amount (%), ranging from 5 to 40) were first characterized by X-ray diffraction (XRD) patterns and Fourier transform infrared (FTIR) spectroscopy. As shown in Fig. 2A, two characteristic peaks at about 13° and 27.2°, are well consistent with (100) and (002) planes of g-C_3N_4, representing in-plane packing and interfacial stacking of g-C_3N_4 sheets, respectively [24]. Compared with pristine g-C_3N_4, the lateral peak of K-C_3N_4 shifts to higher 2θ angles, indicating a progressively smaller stacking distance between nanosheets [23]. SiW_{12}/K-C_3N_4 shows the characteristic peaks
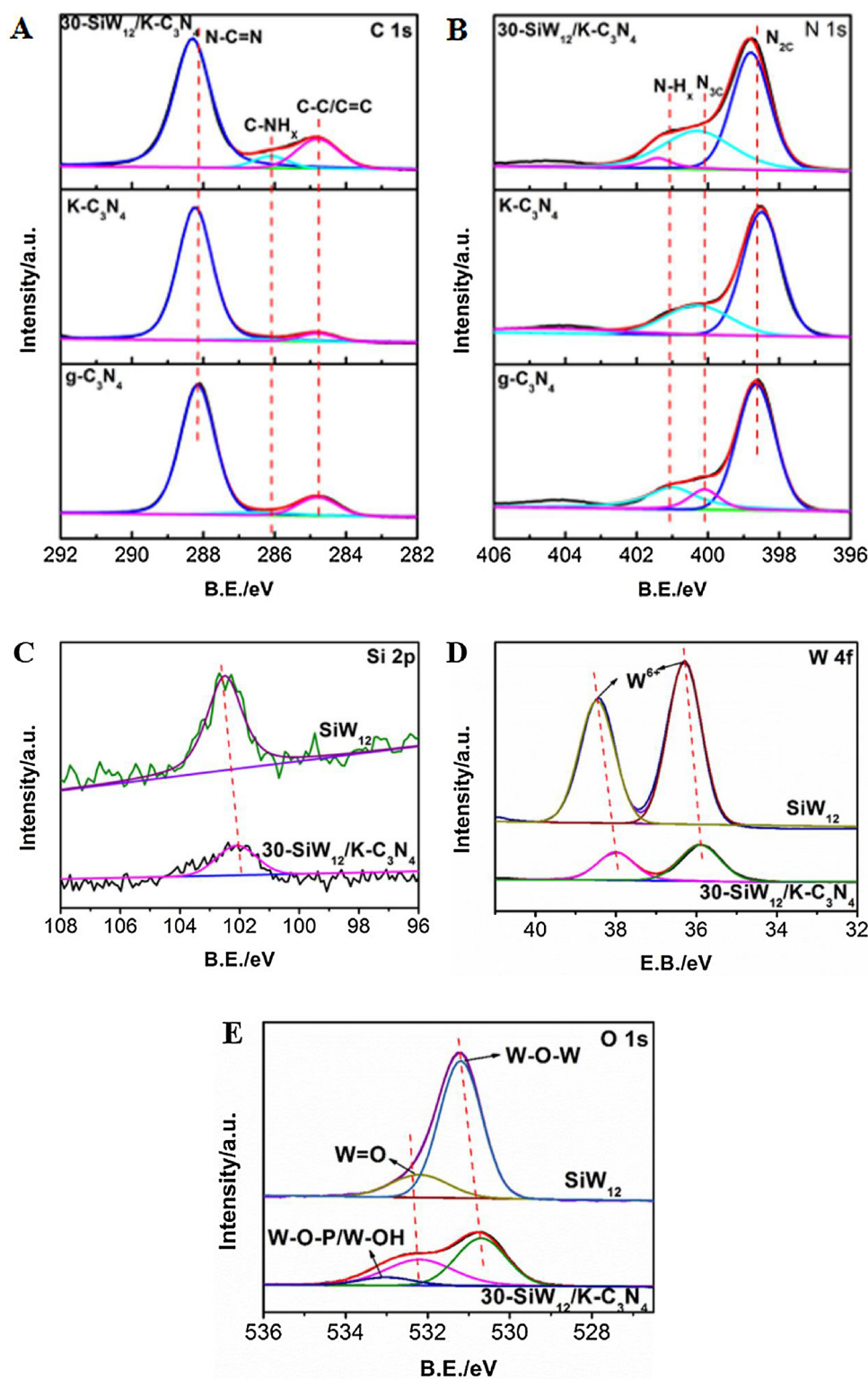
Fig. 3. (A) C 1s and (B) N 1s XPS spectra of g-C_3N_4, K-C_3N_4 and 30-SiW_{12}/K-C_3N_4, (C) Si 2p; (D) W 4f; (E) O 1s XPS spectra of SiW_{12} and 30-SiW_{12}/K-C_3N_4.

of SiW_{12} and K-C_3N_4, indicating that K-C_3N_4 and SiW_{12} are successfully synthesized by taking a phosphate-bridged strategy. When the mass ratio of SiW_{12} to K-C_3N_4 increases from 5% to 40%, the intensity of the SiW_{12}/K-C_3N_4 peak at 27.2° gradually weakens, and the intensity of the SiW_{12}-related peak at 26.4° gradually increases (Fig. S1). This result is attributed to the effect of composition variation in similar hybrid materials on relative diffraction intensity.

Fig. 2B shows the FTIR spectra of pristine g-C_3N_4, K-C_3N_4, SiW_{12}

and 30-SiW_{12}/K-C_3N_4. For pristine g-C_3N_4 (Fig. 2B), the FTIR spectrum showed a peak at 812.7 cm^{-1} typical for the out-of-plane bending mode of heptazine rings, meanwhile peaks located at 900-1800 cm^{-1} stem from N−C=N heterorings in the "melon" framework [23,25]. Multiple broad peaks in the 3000–3500 cm^{-1} region corresponds to the stretching modes of secondary primary amines and absorbed water. For the K-C_3N_4 samples, a distinct change is observed in the FTIR spectra with KOH usage in Fig. 2B, which was the presentation of a new peak at
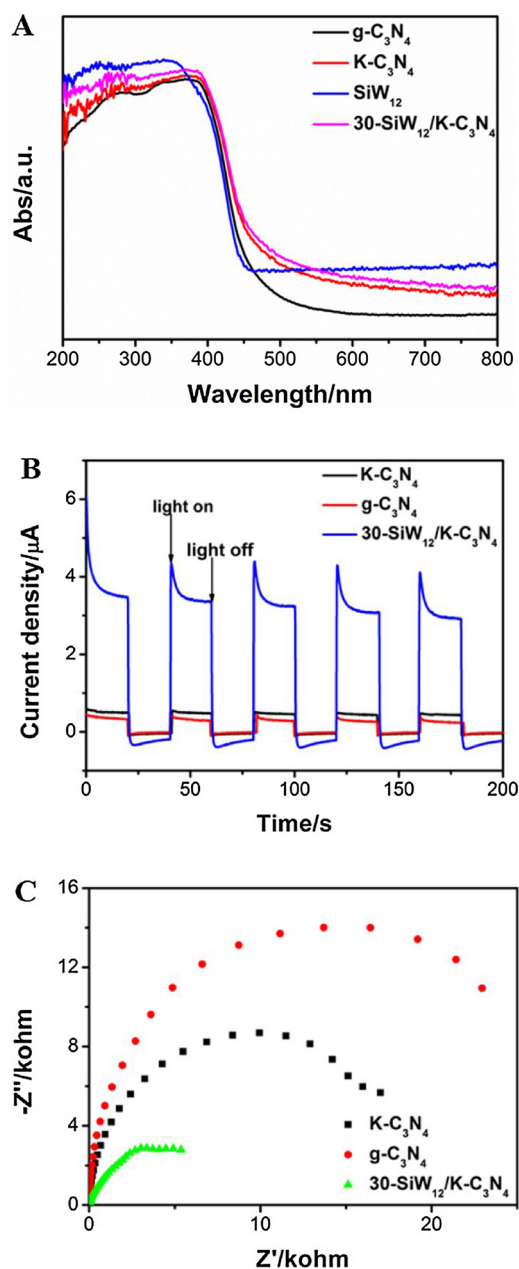
Fig. 4. (A) UV/vis diffuse reflectance spectra of different samples: g-C_3N_4, K-C_3N_4, SiW_{12}, and 30-SiW_{12}/K-C_3N_4; Curves of (B) photocurrent, and (C) Electrochemical impedance spectroscopy response for g-C_3N_4, K-C_3N_4, 30-SiW_{12}/K-C_3N_4 samples in 0.25 M Na_2SO_4 aqueous solution.

Fig. 5. (A) Photocatalytic N_2-fixation activity of x-SiW_{12}/K-C_3N_4 samples with x equal to 0, 5, 10, 20, 30, 40 under visible-light irradiation. (B) photocatalytic N_2-fixation stability test of 30-SiW_{12}/K-C_3N_4 under visible-light irradiation.

band at about 1000–1115 cm^{-1} is attributed to the characteristic absorption peak of phosphate groups, which demonstrate that the main existing form of P is the PO_4^{3-} group (Fig. S3A) [18,33]. Further investigation were carried out using XPS. In Fig. S3B, it was observed that the binding energy of P 2p is centered at about 133.4 eV for P-K-C_3N_4, which is characteristic for P 2p in the phosphate groups. Compared with P-K-C_3N_4, the P 2p peak of 30-SiW_{12}/K-C_3N_4 shifts towards high binding energy, which indicates that the electrons on phosphate radical are transferred to SiW_{12} [18,33]. From both the FTIR and XPS analyses, it is demonstrated that P exists in the form of phosphate groups on the interface of K-C_3N_4 and SiW_{12}, which could act as a favorable charge transport channel in the compound.

3.2. Chemical compositions and states

X-ray photoelectron spectroscopy (XPS) was performed to analyze the state of each element. Firstly, in order to investigate the effects of KOH treatment g-C_3N_4, C 1s and N 1s XPS spectra for pristine g-C_3N_4 and K-C_3N_4 samples were collected. The C 1s XPS spectra for g-C_3N_4 and K-C_3N_4 can be fitted with three peaks at binding energies of around 288.1, 286.4, and 284.7 eV, which corresponds to N−C≡N coordination in the framework of g-C_3N_4, C-NH_X (x = 1, 2) on the edges of heptazine units and adventitious hydrocarbons, respectively [34]. Interestingly, the signal of K-C_3N_4 at 286.4 eV was intensified compared to pristine g-C_3N_4 (Fig. 3A), which may be considered as additional evidence for the formation of cyano groups (as shown by FTIR) owing to C≡N groups possess similar C 1s binding energies to C-NH_X [23,29]. As shown in Fig. 3B, the N 1s XPS spectrum for g-C_3N_4 contained three components at 398.8, 400.1 and 401.2 eV, which are assigned to bi-coordinated (N_{2C}) and tri-coordinated (N_{3C}) nitrogen atoms and NH_X groups in the heptazine framework, respectively. With adding KOH

2177 cm^{-1}, corresponding to the asymmetric stretching vibration of cyano groups (−C≡N) [23,26–28]. This result implies that –C≡N groups was introduced with KOH addition during the synthesis of K-C_3N_4, indicating that more nitrogen vacancies may have been created [29]. As shown in Fig. S2, characteristic SiW_{12} frequencies related to the Keggin unit are 1075, 975, 895, and 762 cm^{-1}, respectively [30]. These frequencies are attributed to vibrations in the Si-O_a bonds of the SiO_3 units, W═O_d bonds, and two W−$O_{b/c}$−W bonds of the Keggin unit [31]. For the 30-SiW_{12}/K-C_3N_4, the characteristic peaks of SiW_{12} and K-C_3N_4 were displayed. This result implies that K-C_3N_4 and SiW_{12} are successfully synthesized by taking a phosphate-bridged strategy and the primary Keggin structure of SiW_{12} remains intact after being introduced into the K-C_3N_4 [32].

In order to confirm the existence of chemical species -O-P-O-, the FTIR and XPS techniques were applied. For SiW_{12}/K-C_3N_4, the new IR
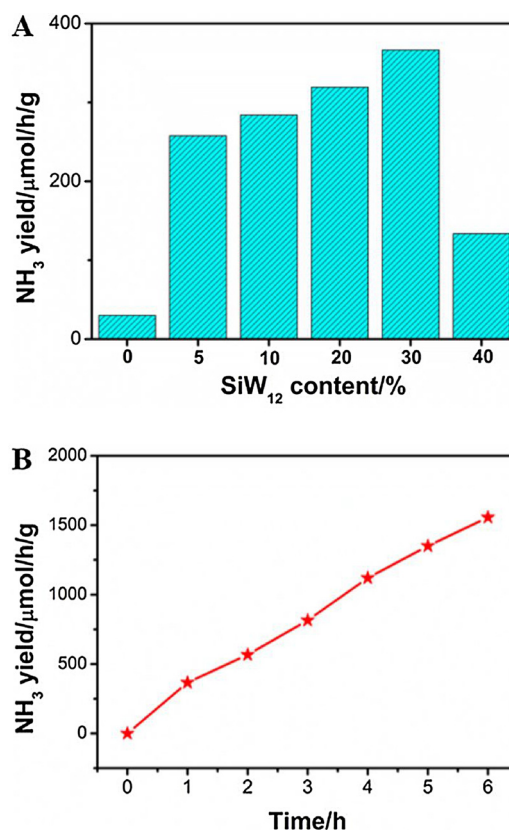
Fig. 6. (A) Linear sweep voltammogram curves of K-C$_3$N$_4$ and SiW$_{12}$/K-C$_3$N$_4$ in the dark; (B) Cyclic voltammetry curve of SiW$_{12}$ in water (0.05 M, pH = 1.5) under Ar and at room temperature; (C) Cyclic voltammetry curve of 30-SiW$_{12}$/K-C$_3$N$_4$ (0.25 M Na$_2$SO$_4$) under Ar and at room temperature; (D) N$_2$-TPD profiles of the as-prepared g-C$_3$N$_4$, K-C$_3$N$_4$ and 30-SiW$_{12}$/K-C$_3$N$_4$ photocatalysts.

during thermal polymerization, the N$_{3C}$ peak presented a small shift to lower binding energy, which may result from the generation of cyano groups whose N 1s binding energy are intermediate between those of

N$_{2C}$ and N$_{3C}$ [23,29]. In order to explore the state of K in K-C$_3$N$_4$, the high resolution of K 2s and K 2p spectrum is shown in the Fig. S4A, B. The binding energy of K 2p$_{3/2}$ and K 2p$_{1/2}$ located at 292.7 and 295.3 eV, which are lower than those of the potassium salt [35], shows that a covalent bond formed between K and g-C$_3$N$_4$. According to the XPS of N 1s and C 1s, the N/C atomic ratios for pristine g-C$_3$N$_4$, K-C$_3$N$_4$ and 30-SiW$_{12}$/K-C$_3$N$_4$ were dropped from 1.32 to 0.98 (Table S1), suggesting the introduction of surface N defects. Further, the intensity of N$_{2C}$ decreases (N$_{2C}$/C atomic ratios dropped from 1.31 to 0.91) (Table S1), strong evidence that N$_{2C}$ vacancies were formed on the surface of K-C$_3$N$_4$ and SiW$_{12}$/K-C$_3$N$_4$ [23]. The above result suggested that KOH treatment with g-C$_3$N$_4$ introduces more nitrogen vacancies, and K is also doped into the framework of g-C$_3$N$_4$.

ESR measurement was employed to further confirm the presence of N-vacancies. As shown in Fig. S5, g-C$_3$N$_4$, K-C$_3$N$_4$ and 30-SiW$_{12}$/K-C$_3$N$_4$ possess one single Lorentzian line centered at the g value of 2.004, which can be ascribed to unpaired electrons in sp^2-carbon atoms of p-bonded aromatic rings due to the formation of carbon-based radicals [11,36–38]. This Lorentzian line was considerably enhanced after doping K and bridging SiW$_{12}$ because the formation of defects increased the number of unpaired electrons.

As for the 30-SiW$_{12}$/K-C$_3$N$_4$ samples, the C 1s and N 1s exhibits a small shift to higher binding energy (Fig. 3A, B), which is attributed to the strong electronic pull of the Keggin unit. Both SiW$_{12}$ and 30-SiW$_{12}$/K-C$_3$N$_4$ samples show one Si 2p XPS peak at 102.09 eV (Fig. 3C) [31]. Besides, the W 4f binding energy of SiW$_{12}$ and SiW$_{12}$/K-C$_3$N$_4$ located at 35.81 eV and 37.92 eV correspond to W^{6+} (Fig. 3D). Further, both SiW$_{12}$ and 30-SiW$_{12}$/K-C$_3$N$_4$ sample shows two O 1s peaks centered at 530.7, 532.7 eV, which is assigned to W−O−W and W=O, respectively (Fig. 3E). Compared with SiW$_{12}$, 30-SiW$_{12}$/K-C$_3$N$_4$ presents a peak at 533.3 eV, which is ascribed to the W-O-P/W-O-H [39]. The above XPS results indicate that SiW$_{12}$ is successfully bridged with K-C$_3$N$_4$ via phosphate and maintains its own stable structure.

3.3. Optical and electrochemical properties

The light absorption property of g-C$_3$N$_4$, SiW$_{12}$, K-C$_3$N$_4$ and 30-SiW$_{12}$/K-C$_3$N$_4$ powders were analyzed via UV–vis/DRS (Fig. 4A). The g-C$_3$N$_4$ exhibits typical semiconductor absorption in the region ranging from 200 nm to 450 nm. And N defects introduced into g-C$_3$N$_4$ by KOH addition during the thermal polymerization of urea dramatically alter their optical properties and light harvesting ability of the samples. It was evident that a progressive red shift in the absorption edge of K-C$_3$N$_4$ was observed, indicating the decline of the band gap energy. Light absorption of SiW$_{12}$ precursor in the region ranging from 200 nm to 415 nm was attributed to charge transfer response from O 2p to W 5d orbit at W=O and W−O−W bonds, respectively [39]. Because of the intense light absorption by SiW$_{12}$ clusters, the light-harvesting capability of 30-SiW$_{12}$/K-C$_3$N$_4$ also increases in the region ranging from 200 nm to 415 nm compared with K-C$_3$N$_4$. Decreased band gap energy and enhanced light harvesting ability are both advantageous to enhance the light utilization efficiency of SiW$_{12}$/K-C$_3$N$_4$. Fig. 4A also shows that the absorption peak related to either SiW$_{12}$ or K-C$_3$N$_4$ is hardly detected in the 30-SiW$_{12}$/K-C$_3$N$_4$ sample, indicating that SiW$_{12}$ is homogeneously distributed throughout the whole hybrid material.

Photoelectrochemistry tests were powerful tools to monitor photo-induced electron-hole pair generation, separation, migration, and capturation by reactive species. Sharp increases in photocurrent responses is observed in all tested working electrodes under the intermittent visible light, as displayed by the photocurrent-time (I-t) curves shown in Fig. 4B. The photo-current values of 30-SiW$_{12}$/K-C$_3$N$_4$ is 3.5 µA, which is much higher than that of K-C$_3$N$_4$ and g-C$_3$N$_4$. Besides, the 30-SiW$_{12}$/K-C$_3$N$_4$ composite is charged after turning off the light, which can be attributed to the electrons on the SiW$_{12}$ are transferred to the K-C$_3$N$_4$, and SiW$_{12}$ acts as a capacitor. To further gain insight into the effect of phosphate bridging on charge carrier transport behavior, the
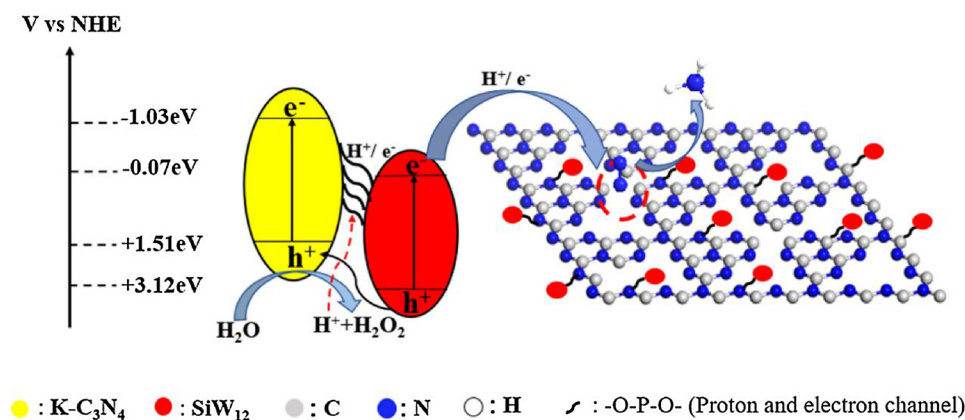
Fig. 7. Schematic illustration of the transfer and separation of photogenerated charges in the -O-P-O- bridged 30-SiW_{12}/K-C_3N_4 nanocomposite and mechanism of photocatalytic nitrogen fixation.

electrochemical impedance spectra (EIS) of g-C_3N_4, K-C_3N_4 and 30-SiW_{12}/K-C_3N_4 were measured. Under light-irradiation, it was observed that the arc radius on the EIS Nyquist plot of g-C_3N_4, K-C_3N_4 and 30-SiW_{12}/K-C_3N_4 were gradually decreased (Fig. 4C), which is due to that phosphate-bridged could decrease photogenerated charge recombination. Normally, the smaller radius represents the smaller charge transfer resistance. Compared with the K-C_3N_4, 30-SiW_{12}/K-C_3N_4 shows a smaller arc radius, implying low charge transfer resistance, which indicates more effective charge carrier transport via the "phosphate bridge" on their hetero-junction interface.

3.4. Photocatalytic performance test

The photocatalytic nitrogen fixation were evaluated under light-irradiation using water as the proton source without any scavenger. A series of controlling experiments indicated that photocatalyst, N_2 and light were all necessary factors for photocatalytic nitrogen fixation (Fig. S6). Without any sacrificial agent, the nitrogen fixation capabilities of pure g-C_3N_4 and K-C_3N_4 were negligible in the water. With the addition of SiW_{12}, the nitrogen fixation efficiency increased gradually, and 30-SiW_{12}/K-C_3N_4 showed the highest photocatalytic nitrogen fixation rate (353.2 $\mu M \, g^{-1} \, h^{-1}$), which was 12 times higher than K-C_3N_4 (Fig. 5A). The photocatalytic efficiency for nitrogen fixation on 30-SiW_{12}/K-C_3N_4 exhibited no significant changes after replacing air with high-purity nitrogen (Fig. S6), revealing that the oxygen in the air had no significant effect on the photocatalytic nitrogen fixation of 30-SiW_{12}/K-C_3N_4. In addition, the cycling tests showed that the nitrogen-fixing performance declined slightly in the first several cycles but remained almost constant at last (Fig. S7A). XRD patterns showed that the structure of 30-SiW_{12}/K-C_3N_4 remained almost unchanged after cycling tests, indicating the stability (Fig. S7B). Moreover, the nitrogen fixation performance showed a linear increase along with the reaction time, indicating the favorable stability of 30-SiW_{12}/K-C_3N_4 for the nitrogen fixation (Fig. 5B).

3.5. Catalytic mechanism

In order to investigate the effects of SiW_{12} and K doping on the nitrogen fixation further, electrochemical experiments and N_2-TPD were employed. Fig. 6A shows the linear sweep voltammogram (LSV) curves of the electrodes with the K-C_3N_4 and 30-SiW_{12}/K-C_3N_4 in the dark. The onset potential of K-C_3N_4 was at approximately 1.94 V vs. NHE in the dark. Compared with K-C_3N_4, not only did the onset potential of 30-SiW_{12}/K-C_3N_4 negatively shift to 1.74 V vs. NHE, but also the current density was greatly enhanced, which clearly revealed that SiW_{12} could improve the performance of water oxidation [40]. Further, in this reaction system, holes may oxidize water into hydrogen peroxide

by the two-electron process rather than directly oxidize water into oxygen [41], since hydrogen peroxide was detected over the K-C_3N_4 (27.5 μM/L) and SiW_{12}/K-C_3N_4 (42.3 μM/L) (Figure S8). Based on this result, it is clear that the bridged SiW_{12} would enhance the performance of water oxidation. Cyclic voltammograms of SiW_{12} shows that reversible one-electron redox occurred on the surface of SiW_{12} reactions at -0.035 V (peak1) and -0.266 V (peak2) (0.05 M SiW_{12} (pH = 1.5)) (Fig. 6B) [42], while the reduction potential of 30-SiW_{12}/K-C_3N_4 located at -0.06 V (peak3) and -0.36 V (peak4) (0.25 M Na_2SO_4 (pH = 6.8)) corresponded to two-electron redox reaction (Fig. 6C), implying that 30-SiW_{12}/K-C_3N_4 could act as good containers of electrons and protons, so as to provide protons for the N_2 reduction. Furthermore, the photogenerated electron and protons from water deposed could be transferred by phosphate bridge and stored in the POM [17,43], as heteropolyblue form in Ar atmosphere, but these "stored" electron and protons could be coupled to the actived N_2 absorbed on SiW_{12}/K-C_3N_4 (shown in supporting Fig. S9).

As shown in nitrogen temperature programmed desorption test (N_2-TPD, Fig. 6D), the desorption peaks at about 100 °C and 150 °C corresponded to the physical adsorption of N_2, while that of 350 °C and 450 °C are the desorption peaks of nitrogen chemisorption. Compared with g-C_3N_4 and SiW_{12}, K-C_3N_4 and SiW_{12}/K-C_3N_4 exhibited much higher adsorption of N_2. It suggests that K doping and bridging SiW_{12} could improve the adsorption and activation of N_2. In addition, compared with 30-SiW_{12}/K-C_3N_4, the nitrogen-fixing performance of 30-SiW_{12}/g-C_3N_4 decreased obviously, indicating that K doping promotes nitrogen reduction. Thus, the combination of SiW_{12}/K-C_3N_4 based on phosphate bridge leads to significant enhancement of adsorption of N_2 and enhanced NH_3 production.

Based on these results, we supposed that there are two reasons for the enhanced photocatalytic activity of SiW_{12}/K-C_3N_4 for photocatalytic N_2 fixation, and a schematic mechanism is shown in Fig. 7. First, more protons and electrons are supplied for the nitrogen fixation in the photocatalytic reaction over the SiW_{12}/K-C_3N_4. Under the light irradiation, photogenerated electrons from K-C_3N_4 are efficiently transfred to SiW_{12}, and holes are transformed with an apposite path, due to the "phosphate bridge" on the interface as an electron transport chain. The photogenerated electron and protons from water dissociation could transfer along the phosphate bridge and store in the POM, as heteropolyblue form in Ar atmosphere, while these "stored" electron and protons could couple with the actived N_2 absorbed on SiW_{12}/K-C_3N_4. Furthermore, phosphate anions, as efficient electron transport chains, promote photogenerated electrons transferring from K-C_3N_4 to SiW_{12}, which enhances separation efficiency of charge carriers. Second, both K doping and bridging SiW_{12} improves the adsorption and activation of nitrogen, which are beneficial to the N_2 fixation reaction.

4. Conclusion

In summary, phosphate-bridged POM/K-C$_3$N$_4$ nanocomposites have been successfully constructed by a wet-chemical process. By introducing the "phosphate bridge" on the interface as an electron transport chain, the charge spatial separation was obviously enhanced. It was attributed to the fact that phosphate bridge, as an excellent electron transport chain, can rapidly transfer photogenerated electrons from K-C$_3$N$_4$ to SiW$_{12}$, thus greatly reducing the recombination rates of photogenerated carries. Furthermore, bridged SiW$_{12}$ not only enhances the oxidation ability of water, but also increases the rate of nitrogen-fixing reaction due to that these "stored" electron and protons in SiW$_{12}$ could be fastly coupled to the actived N$_2$ absorbed on K-C$_3$N$_4$. Both K doping and bridging SiW$_{12}$ improve the adsorption and activation of nitrogen, which was obserbed by N$_2$-TPD. Hence, the SiW$_{12}$/K-C$_3$N$_4$ nanocomposites based on phosphate bridge achieved a high nitrogen fixation efficiency (353.2 μM g^{-1} h^{-1}). This work would supply a novel approach to design and synthesize other visible-light heterojunction nanocomposite photocatalysts with good performance.

Acknowledgement

Appendix A. Supplementary data

Supplementary material related to this article can be found, in the online version, at doi:https://doi.org/10.1016/j.apcatb.2018.08.012.

References

[1] B. Askevold, J.T. Nieto, S. Tussupbayev, M. Diefenbach, E. Herdtweck, M.C. Holthausen, S. Schneider, Ammonia formation by metal–ligand cooperative hydrogenolysis of a nitrido ligand, Nat. Chem. 3 (2011) 532–537.

[2] O. Einsle, F.A. Tezcan, L.A. Andrade, B. Schmid, M. Yoshida, J.B. Howard, D.C. Rees, Nitrogenase MoFe-Protein at 1.16 Å resolution: a central ligand in the FeMo-Cofactor, Science 297 (2002) 1696–1700.

[3] I. Rafiqul, C. Weber, B. Lehmann, A. Voss, Energy efficiency improvements in ammonia production—perspectives and uncertainties, Energy 30 (2005) 2487–2504.

[4] B.M. Hoffman, D. Lukoyanov, Z.Y. Yang, D.R. Dean, L.C. Seefeldt, Mechanism of nitrogen fixation by nitrogenase: the next stage, Chem. Rev. 114 (2014) 4041–4062.

[5] C.J.M. van der Ham, M.T.M. Koper, D.G.H. Hetterscheid, Challenges in reduction of dinitrogen by proton and electron transfer, Chem. Soc. Rev. 43 (2014) 5183–5191.

[6] Z. Li, Y. Qu, K. Hu, M. Humayun, S. Chen, L. Jing, Improved photoelectrocatalytic activities of BiOCl with high stability for water oxidation and MO degradation by coupling RGO and modifying phosphate groups to prolong carrier lifetime, Appl. Catal. B- Environ. 203 (2017) 355–362.

[7] X. Li, W. Wang, D. Jiang, S. Sun, L. Zhang, X. Sun, Efficient solar-driven nitrogen fixation over carbon-tungstic-Acid hybrids, Chem. Eur. J. 22 (2016) 13819–13822.

[8] X. Li, D. Jiang, L. Zhang, S. Sun, W. Wang, Enhanced nitrogen photofixation over LaFeO$_3$ via acid treatment, ACS Sustain. Chem. Eng. 5 (2017) 9965–9971.

[9] S. Sun, X. Li, W. Wang, L. Zhang, X. Sun, Photocatalytic robust solar energy reduction of dinitrogen to ammonia on ultrathin MoS$_2$, Appl. Catal. B- Environ. 200 (2017) 323–329.

[10] S. Sun, Q. An, W. Wang, L. Zhang, J. Liu, W.A. Goddard Iii, Efficient photocatalytic reduction of dinitrogen to ammonia on bismuth monoxide quantum dots, J. Mater. Chem. A Mater. Energy Sustain. 5 (2017) 201–209.

[11] G. Dong, W. Ho, C. Wang, Selective photocatalytic N$_2$ fixation dependent on g-C$_3$N$_4$ induced by nitrogen vacancies, J. Mater. Chem. A Mater. Energy Sustain. 3 (2015) 23435–23441.

[12] W. Zhao, J. Zhang, X. Zhu, M. Zhang, J. Tang, M. Tan, Y. Wang, Enhanced nitrogen photofixation on Fe-doped TiO$_2$ with highly exposed (101) facets in the presence of ethanol as scavenger, Appl. Catal. B- Environ. 144 (2014) 468–477.

[13] Q. Liu, L. Ai, J. Jiang, MXene-derived TiO$_2$@C/g-C$_3$N$_4$ heterojunctions for highly efficient nitrogen photofixation, J. Mater. Chem. A Mater. Energy Sustain. 6 (2018) 4102–4110.

[14] X. Li, X. Sun, L. Zhang, S. Sun, W. Wang, Efficient photocatalytic fixation of N$_2$ by KOH-treated g-C$_3$N$_4$, J. Mater. Chem. A Mater. Energy Sustain. 6 (2018) 3005–3011.

[15] J.K. Hurst, Chemistry. In pursuit of water oxidation catalysts for solar fuel production, Science 328 (2010) 315–316.

[16] S. Zhao, X. Zhao, H. Zhang, J. Li, Y. Zhu, Covalent combination of polyoxometalate and graphitic carbon nitride for light-driven hydrogen peroxide production, Nano

Energy 35 (2017) 405–414.

[17] M.D. Symes, L. Cronin, Decoupling hydrogen and oxygen evolution during electrolytic water splitting using an electron-coupled-proton buffer, Nat. Chem. 5 (2013) 403–409.

[18] N. Sun, Y. Qu, S. Chen, R. Yan, M. Humayun, Y. Liu, L. Bai, L. Jing, H. Fu, Efficient photodecomposition of 2,4-dichlorophenol on recyclable phase-mixed hierarchically structured Bi$_2$O$_3$ coupled with phosphate-bridged nano-SnO$_2$, Environ. Sci. Nano 4 (2017) 1147–1154.

[19] C. Liu, L. Jing, L. He, Y. Luan, C. Li, Phosphate-modified graphitic C$_3$N$_4$ as efficient photocatalyst for degrading colorless pollutants by promoting O$_2$ adsorption, Chem. Commun. 50 (2014) 1999–2001.

[20] C. Liu, C. Li, X. Fu, F. Raziq, Y. Qu, L. Jing, Synthesis of silicate-bridged ZnO/g-C$_3$N$_4$ nanocomposites as efficient photocatalysts and its mechanism, RSC Adv. 5 (2015) 37275–37280.

[21] Z. Li, Y. Luan, Y. Qu, L. Jing, Modification strategies with inorganic acids for efficient photocatalysts by promoting the adsorption of O$_2$, ACS. Appl. Mater. Interface 7 (2015) 22727–22740.

[22] M. Long, J. Brame, F. Qin, J. Bao, Q. Li, P.J. Alvarez, Phosphate changes effect of humic acids on TiO$_2$ photocatalysis: from inhibition to mitigation of electron-hole recombination, Environ. Sci. Technol. 51 (2017) 514–521.

[23] H. Yu, R. Shi, Y. Zhao, T. Bian, Y. Zhao, C. Zhou, G.I.N. Waterhouse, L.Z. Wu, C.H. Tung, T. Zhang, Alkali-assisted synthesis of nitrogen deficient graphitic carbon nitride with tunable band structures for efficient visible-light-Driven hydrogen evolution, Adv. Mater. (2017) 29.

[24] A. Thomas, A. Fischer, F. Goettmann, M. Antonietti, J.-O. Müller, R. Schlögl, J.M. Carlsson, Graphitic carbon nitride materials: variation of structure and morphology and their use as metal-free catalysts, J. Mater. Chem. 18 (2008) 4893.

[25] Y. Cui, Y. Tang, X. Wang, Template-free synthesis of graphitic carbon nitride hollow spheres for photocatalytic degradation of organic pollutants, Mater. Lett. 161 (2015) 197–200.

[26] E. Irran, B. Jürgens, W. Schnick, Synthesis, crystal structure determination from X-ray powder diffractometry and vibrational spectroscopy of the tricyanomelamintemonohydrates M$_3$[C$_6$N$_9$]·H$_2$O (M = K, Rb), Solid. State. Sci. 4 (2002) 1305–1311.

[27] W. Lei, D. Portehault, R. Dimova, M. Antonietti, Boron carbon nitride nanostructures from salt melts: tunable water-soluble phosphors, J. Am. Chem. Soc. 133 (2011) 7121–7127.

[28] Y. Cui, Z. Ding, X. Fu, X. Wang, Construction of conjugated carbon nitride nanoarchitectures in solution at low temperatures for photoredox catalysis, Angew. Chem. Int. Ed. Engl. 51 (2012) 11814–11818.

[29] H. Gao, S. Yan, J. Wang, Y.A. Huang, P. Wang, Z. Li, Z. Zou, Towards efficient solar hydrogen production by intercalated carbon nitride photocatalyst, Phys. Chem. Chem. Phys. 15 (2013) 18077–18084.

[30] A.K. Cuentas-Gallegos, A. Zamudio-Flores, M. Casas-Cabanas, Dispersion of SiW$_{12}$ nanoparticles on highly oxidized multiwalled carbon nanotubes and their electrocatalytic behavior, J. Nano. Res. 14 (2011) 11–18.

[31] Y. Wang, C. Guo, Y. Chen, C. Hu, W. Yu, Self-assembled multilayer films based on a Keggin-type polyoxometalate and polyaniline, J. Colloid Interface Sci. 264 (2003) 176–183.

[32] H. Wang, C. Wang, Y. Yang, M. Zhao, Y. Wang, H$_3$PW$_{12}$O$_{40}$/mpg-C$_3$N$_4$ as an efficient and reusable bifunctional catalyst in one-pot oxidation–Knoevenagel condensation tandem reaction, Catal. Sci. Technol. 7 (2017) 405–417.

[33] C. Liu, F. Raziq, Z. Li, Y. Qu, A. Zada, L. Jing, Synthesis of TiO$_2$/g-C$_3$N$_4$ nanocomposites with phosphate–oxygen functional bridges for improved photocatalytic activity, Chin. J. Catal. 38 (2017) 1072–1078.

[34] L. Lin, H. Ou, Y. Zhang, X. Wang, Tri-s-triazine-Based Crystalline Graphitic Carbon Nitrides for Highly Efficient Hydrogen Evolution Photocatalysis, ACS Catal. 6 (2016) 3921–3931.

[35] K.H. Park, B.H. Kim, S.H. Song, J. Kwon, B.S. Kong, K. Kang, S. Jeon, Exfoliation of non-oxidized graphene flakes for scalable conductive film, Nano Lett. 12 (2012) 2871–2876.

[36] Y. Hou, J. Yang, C. Lei, B. Yang, Z. Li, Y. Xie, X. Zhang, L. Lei, J. Chen, Nitrogen vacancy structure driven photoeletrocatalytic degradation of 4-Chlorophenol using porous graphitic carbon nitride nanosheets, ACS Sustain. Chem. Eng. 6 (2018) 6497–6506.

[37] J. Li, J. Zhang, F. Zhou, H. Zhang, J. Bai, Y. Wang, H. Wang, Preparation of N-vacancy-doped g-C$_3$N$_4$ with outstanding photocatalytic H$_2$O$_2$ production ability by dielectric barrier discharge plasma treatment, Chin. J. Cata. 39 (2018) 1090–1098.

[38] X. Qu, S. Hu, P. Li, Z. Li, H. Wang, H. Ma, W. Li, The effect of embedding N vacancies into g-C$_3$N$_4$ on the photocatalytic H$_2$O$_2$ production ability via H$_2$ plasma treatment, Diamond Relat. Mater. 86 (2018) 159–166.

[39] K. Li, L. Yan, Z. Zeng, S. Luo, X. Luo, X. Liu, H. Guo, Y. Guo, Fabrication of H$_3$PW$_{12}$O$_{40}$-doped carbon nitride nanotubes by one-step hydrothermal treatment strategy and their efficient visible-light photocatalytic activity toward representative aqueous persistent organic pollutants degradation, Appl. Catal. B-Environ. 156–157 (2014) 141–152.

[40] S. Li, J.A. Willoughby, O.J. Rojas, Oil-in-water emulsions stabilized by carboxymethylated lignins: properties and energy prospects, ChemSusChem 9 (2016) 2460–2469.

[41] J. Liu, Y. Liu, N. Liu, Y. Han, X. Zhang, H. Huang, Y. Lifshitz, S.T. Lee, J. Zhong, Z. Kang, Metal-free efficient photocatalyst for stable visible water splitting via a two-electron pathway, Science 347 (2015) 970–974.

[42] B. Rausch, M.D. Symes, G. Chisholm, L. Cronin, Decoupled catalytic hydrogen evolution from a molecular metal oxide redox mediator in water splitting, Science 345 (2014) 1326–1330.

[43] S. Zeng, L. Zhang, W. Wang, D. Shao, H. Hao, Hydrogen evolution based on the electrons/protons stored on amorphous TiO$_2$, Phys. Chem. Chem. Phys. 19 (2017) 29053–29056.